

Surface stress effects on the resonant properties of silicon nanowires

Harold S. Park^{a)}

Department of Mechanical Engineering, University of Colorado, Boulder, Colorado 80309, USA

(Received 15 February 2008; accepted 11 April 2008; published online 16 June 2008)

The purpose of the present work is to quantify the coupled effects of surface stresses and boundary conditions on the resonant properties of silicon nanowires. We accomplish this by using the surface Cauchy–Born model, which is a nonlinear, finite deformation continuum mechanics model that enables the determination of the nanowire resonant frequencies including surface stress effects through solution of a standard finite element eigenvalue problem. By calculating the resonant frequencies of both fixed/fixed and fixed/free $\langle 100 \rangle$ silicon nanowires with unreconstructed $\{100\}$ surfaces using two formulations, one that accounts for surface stresses and one that does not, it is quantified how surface stresses cause variations in nanowire resonant frequencies from those expected from continuum beam theory. We find that surface stresses significantly reduce the resonant frequencies of fixed/fixed nanowires as compared to continuum beam theory predictions, while small increases in resonant frequency with respect to continuum beam theory are found for fixed/free nanowires. It is also found that the nanowire aspect ratio, and not the surface area to volume ratio, is the key parameter that correlates deviations in nanowire resonant frequencies due to surface stresses from continuum beam theory. © 2008 American Institute of Physics.

[DOI: [10.1063/1.2939576](https://doi.org/10.1063/1.2939576)]

I. INTRODUCTION

Nanowires have been among the most studied nanomaterials in recent years. The intense interest in nanowires has emerged for a variety of reasons, foremost because their small sizes often lead to unique physical properties that are not observed in the corresponding bulk material. Nonbulk phenomena have been observed in the mechanical, electrical, thermal, and optical properties of both metallic and semiconducting nanowires.¹ These unique properties have therefore generated significant interest in using nanowires as the basic building blocks of future multifunctional nanoelectromechanical systems (NEMS).²

With the recent explosion in NEMS research, silicon nanowires, or silicon-based compounds (SiC, SiN), have been utilized most frequently as the basic building block of NEMS. There are multiple reasons for this, including the ability to micromachine nanometer-scale silicon nanowires,³ and the fact that silicon is the fundamental material in the microelectronics industry coupled with its potential as an optoelectronic material.⁴ Silicon nanowire-based NEMS have been studied in a wide variety of applications, including high frequency resonators for next-generation wireless devices,² force sensors,⁵ electrometers for charge measurement,⁶ and chemical and biological mass sensors.⁷

Many of these applications^{2,5,7} require precise knowledge of the nanowire resonant frequency, or variations in the resonant frequency due to environmental changes that are to be measured, i.e., adsorbed mass for mass sensing. However, the understanding and design of such NEMS is significantly complicated by the fact that the elastic properties, and thus the resonant frequencies of nanowires are known to differ from those of the bulk material.

Nanowire elastic properties are different from those of bulk materials due to the presence of free surfaces. In particular, surface atoms are subject to surface stresses.^{8–10} Surface stresses on nanomaterials arise due to an imbalance in the forces acting on surface atoms due to their lack of bonding neighbors. Because surface atoms have a different bonding environment than atoms that lie within the material bulk, the elastic properties of surfaces differ from those of the bulk material, and the effects of the difference between surface and bulk elastic properties on the effective elastic properties of the nanowire become magnified with decreasing structural size or increasing surface area to volume ratio.

The elastic properties of silicon nanowires have been theoretically predicted to show a strong size dependence.^{11,12} Many experimental studies, either through resonant-based testing^{7,13} or atomic force microscope (AFM)-based bending^{14,15} of the elastic properties of silicon nanowires with cross-sectional sizes larger than 50 nm, where surface effects are not expected to be significant. However, experiments using nanowires with cross-sectional sizes less than 20 nm (Refs. 16–18) agree with theoretical predictions¹¹ that the Young's modulus of silicon decreases with decreasing size. We note that such size dependence has also been experimentally observed in metallic nanowires.^{19,20}

Therefore, the purpose of this work is to quantify how surface stresses impact the resonant properties of silicon nanowires. In particular, we study $\langle 100 \rangle$ silicon nanowires with unreconstructed $\{100\}$ surfaces that have cross-sectional sizes ranging from 10 to 30 nm using both the fixed/fixed and fixed/free beam-type boundary conditions that are prevalent in NEMS design. The size range for the nanowire cross sections is deliberately chosen to bridge the gap between size scales that can be studied using atomistic calculations, and those which are commonly studied experimentally.

^{a)}Electronic mail: harold.park@colorado.edu.

While it is known that the $\{100\}$ surfaces of silicon tend to undergo dimerized reconstructions,²¹ we focus on the unreconstructed $\{100\}$ surfaces in the present work. In doing so, we note that the ideal $1 \times 1\{100\}$ and 2×1 dimerized $\{100\}$ surfaces of silicon both experience a compressive surface stress²¹ leading to tensile strain. However, the compressive surface stress experienced by the 2×1 dimerized silicon nanowires is not as large as that of the unreconstructed $\{100\}$ surfaces due to the fact that the dimerized surface atoms have three nearest neighbors, as compared to only two for the unreconstructed surface atoms. Therefore, it is expected that the trends discussed in the present work would hold qualitatively for dimerized silicon nanowires, with the effects of the surface stress being slightly mitigated as compared to the unreconstructed surfaces.

We address this goal by utilizing the recently developed surface Cauchy–Born (SCB) model.^{22,23} The uniqueness of the SCB model as compared to other surface elastic models^{24–27} is that it enables, by correctly accounting for surface stress effects on nanomaterials, the solution of three-dimensional nanomechanical boundary value problems for displacements, stresses and strains in nanomaterials using standard nonlinear finite element (FE) techniques, where the nonlinear material constitutive response obtained directly from realistic interatomic potentials such as the Tersoff potential.²⁸

The resonant properties of the silicon nanowires are determined by solving a standard FE eigenvalue problem for the resonant frequencies and associated mode shapes, with full accounting for surface stress effects through the FE stiffness matrix. We quantify the effects of surface stress on the fundamental resonant frequency for both fixed/free and fixed/fixed boundary conditions as functions of geometry, size, and surface area to volume ratio. We further compare the results to those obtained on the same geometries using the standard bulk Cauchy–Born material, which does not account for surface stress effects, to quantify how surface stresses cause the resonant frequencies of silicon nanowires to deviate from those predicted using continuum beam theory.

II. THEORY

A. Bulk Cauchy–Born model for silicon

The bulk Cauchy–Born (BCB) model is a hierarchical multiscale assumption that enables the calculation of continuum stress and moduli directly from atomistic principles.²⁹ The BCB formulation in this work for silicon closely mirrors that of Tang *et al.*³⁰ and Park and Klein.³¹ Because the SCB model for silicon is much easier to understand once the bulk formulation is presented, we present an abbreviated version of the BCB formulation later.

In the present work, we utilize the T3 form of the Tersoff potential²⁸ and the resulting parameters. The T3 is named as such due to the fact that two earlier versions of the Tersoff potential suffered from various shortcomings, including not predicting diamond as the ground state of silicon, inaccura-

cies in the bulk elastic constants, and inaccurate modeling of the $\{100\}$ surfaces of silicon.²¹ The T3 potential energy U can be written as

$$U = \frac{1}{2} \sum_{i \neq j} V_{ij},$$

$$V_{ij} = f_C(r_{ij})[f_R(r_{ij}) + b_{ij}f_A(r_{ij})], \quad (1)$$

where r_{ij} is the distance between atoms i and j , f_C is a cutoff function, which is used to ensure that the Tersoff potential is effectively a nearest neighbor potential, f_R is a repulsive function, f_A is an attractive function, and b_{ij} is the bond order function, which is used to modify the bond strength depending on the surrounding environment.

The various functions all have analytic forms, which are given as

$$f_R(r_{ij}) = A e^{-\lambda r_{ij}}, \quad (2)$$

$$f_A(r_{ij}) = -B e^{-\mu r_{ij}}, \quad (3)$$

$$b_{ij} = (1 + \beta^n \zeta_{ij}^n)^{-1/2n}, \quad (4)$$

where

$$\zeta_{ij} = \sum_{k \neq i, j} f_C(r_{ik}) g(\theta_{ijk}), \quad (5)$$

and

$$g(\theta_{ijk}) = 1 + \frac{c^2}{d^2} - \frac{c^2}{d^2 + (h - \cos \theta_{ijk})^2}, \quad (6)$$

where θ_{ijk} represents the angle between a triplet of atoms $i-j-k$.

In order to turn the atomistic potential energy into a form suitable for the BCB approximation, two steps are taken. First, the potential energy is converted into a strain energy density through normalization by a representative atomic volume Ω_0 ; Ω_0 can be calculated for diamond cubic (DC) lattices such as silicon by noting that there are eight atoms in a DC unit cell of volume a_0^3 , where $a_0 = 5.432 \text{ \AA}$ is the silicon lattice parameter. Thus, $\Omega_0 = 8/a_0^3$ for a $\langle 100 \rangle$ oriented silicon crystal. Second, the neighborhood surrounding each atom is constrained to deform homogeneously via continuum mechanics quantities such as the deformation gradient \mathbf{F} , or the stretch tensor $\mathbf{C} = \mathbf{F}^T \mathbf{F}$. It is critical to note that due to the usage of nonlinear kinematics through \mathbf{F} and \mathbf{C} , the BCB model is a finite deformation, nonlinearly elastic constitutive model that explicitly represents the stretching and rotation of bonds undergoing large deformation.

Silicon is well known to occur naturally in the DC lattice structure, which is formed through two interpenetrating face-centered-cubic (fcc) lattices, where the two fcc lattices are offset by a factor of $(a_0/4, a_0/4, a_0/4)$. The DC lattice is shown in Fig. 1, which illustrates the interpenetrating fcc lattices. The complication in modeling DC lattices, which will be resolved later, is that the interpenetrating fcc lattices must be allowed to translate with respect to each other. This key restriction can be accommodated through a five-atom

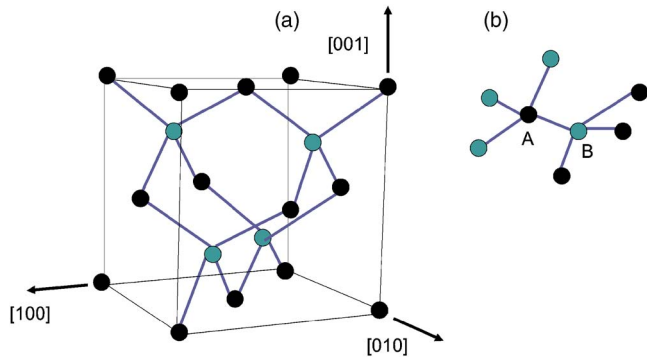


FIG. 1. (Color online) Illustration of the diamond cubic lattice structure of silicon. Black atoms represent standard fcc unit cell atoms, while green atoms represent the interpenetrating fcc lattice. The drawn bonds connect atoms in fcc lattice B to atoms in fcc lattice A.

unit cell, i.e., atom A and its four neighbors in Fig. 1(b), for which the corresponding Tersoff strain energy density Φ can be written as

$$\Phi[r_{1j}(\mathbf{C})] = \frac{1}{2\Omega_0} \sum_{j=2}^5 V_{1j}[r_{1j}(\mathbf{C})], \quad (7)$$

where $i=1$ in Eq. (7) because atom i is considered the center of the unit cell (see Fig. 1), and the summation goes over the four nearest neighbor bonds $j=2,3,4,5$. The full expression for the strain energy density $\Phi(r_{1j})$ can be written as

$$\begin{aligned} \Phi[r_{1j}(\mathbf{C})] = & \frac{V_{1j}}{2\Omega_0} = A e^{-\lambda r_{1j}(\mathbf{C})} - B e^{-\mu r_{1j}(\mathbf{C})} \\ & \times \{1 + \beta^n [\sum_{k \neq i,j} g(\theta_{1jk})]^n\}^{-1/2n}, \end{aligned} \quad (8)$$

where again the multibody effects of the bonding environment are captured through the $g(\theta_{1jk})$ term. We enable the interpenetrating fcc lattices to translate with respect to each other by introducing an internal degree of freedom Ξ associated with all neighboring atoms of atom A in Fig. 1(b) through the modified bond lengths r_{1j} as

$$r_{1j} = |\mathbf{r}_{1j}| = |\mathbf{F}(\mathbf{R}_{1j} + \Xi)|, \quad j = 2,3,4,5, \quad (9)$$

where \mathbf{r}_{1j} is the deformed bond vector, \mathbf{R}_{1j} is the undeformed bond vector between atoms 1 and j and Ξ is the shift introduced between the two interpenetrating fcc lattices (i.e., lattices A and B in Fig. 1) in the undeformed configuration.

The incorporation of the internal degrees of freedom and writing the bond lengths in terms of \mathbf{F} results in a modified strain energy density function as

$$\Phi(\mathbf{C}) = \tilde{\Phi}[\mathbf{C}, \Xi(\mathbf{C})]. \quad (10)$$

Using standard continuum mechanics relationships, we can calculate the second Piola–Kirchhoff stress (PK2) as

$$\frac{1}{2}\mathbf{S} = \frac{\partial \Phi}{\partial \mathbf{C}} = \frac{\partial \tilde{\Phi}}{\partial \mathbf{C}} + \frac{\partial \tilde{\Phi}}{\partial \Xi} \frac{\partial \Xi}{\partial \mathbf{C}}. \quad (11)$$

To keep the crystal at an energy minimum, the internal degrees of freedom are constrained to deform according to Ξ^* , which leads to the following relationship:

$$\frac{\partial \tilde{\Phi}}{\partial \Xi^*} = 0, \quad (12)$$

and changes the final expression for the PK2 stress to

$$\mathbf{S} = 2 \frac{\partial \tilde{\Phi}}{\partial \mathbf{C}}. \quad (13)$$

The spatial tangent modulus can be similarly calculated using standard continuum mechanics relations, and can be written as

$$\mathcal{C}_{IJKL} = M_{IJKL} - A_{IJp} A_{KLq} (\mathbf{D}^{-1})_{pq}, \quad (14)$$

where

$$\begin{aligned} M_{IJKL} &= 4 \frac{\partial^2 \tilde{\Phi}}{\partial C_{IJ} \partial C_{KL}}, \\ D_{pq} &= \frac{\partial^2 \tilde{\Phi}}{\partial \Xi_p^* \partial \Xi_q^*}, \\ A_{IJp} &= 2 \frac{\partial^2 \tilde{\Phi}}{\partial C_{IJ} \partial \Xi_p^*}. \end{aligned} \quad (15)$$

B. Surface Cauchy–Born model for silicon

In this section, we present the formulation by which surface stresses are accounted for through an extension of the BCB model we call the SCB model. The SCB model was developed previously for both fcc crystals^{22,23} and for DC lattices.³¹ We therefore briefly summarize the relevant aspects of the SCB model for silicon³¹ in this section. We first note that the total energy of a nanostructure can be written as the sum of bulk and surface terms

$$\sum_{\alpha=1}^{n_{\text{atoms}}} U_{\alpha}(r) \approx \int_{\Omega_0^{\text{bulk}}} \Phi(\mathbf{C}) d\Omega + \int_{\Gamma_0} \gamma(\mathbf{C}) d\Gamma, \quad (16)$$

where $U_{\alpha}(r)$ represents the potential energy for each atom α , $\Phi(\mathbf{C})$ is the bulk energy density previously defined in Eq. (8), and $\gamma(\mathbf{C})$ is the surface energy density. The issue then is to determine a representation for the surface unit cell that will be used to calculate the surface energy density $\gamma(\mathbf{C})$.

We accomplish this through the nine atom surface unit cell for unreconstructed {100} silicon surfaces shown in Fig. 2. The rationale for this particular unit cell arises because atoms 2 and 6 both have a full complement of neighbors, and thus represent a distinct fcc lattice B. The atoms neighboring atoms 2 and 6 therefore must be part of the interpenetrating fcc lattice A, and thus should be able to translate with respect to atoms 2 and 6. Therefore, we assign an internal degree of freedom Ξ^s , where the superscript s designates an internal surface degree of freedom, to all the black atoms (1,3,4,7,8,9) of fcc lattice A in Fig. 2.

The resulting strain energy density γ for the surface unit cell seen in Fig. 2 can thus be written as

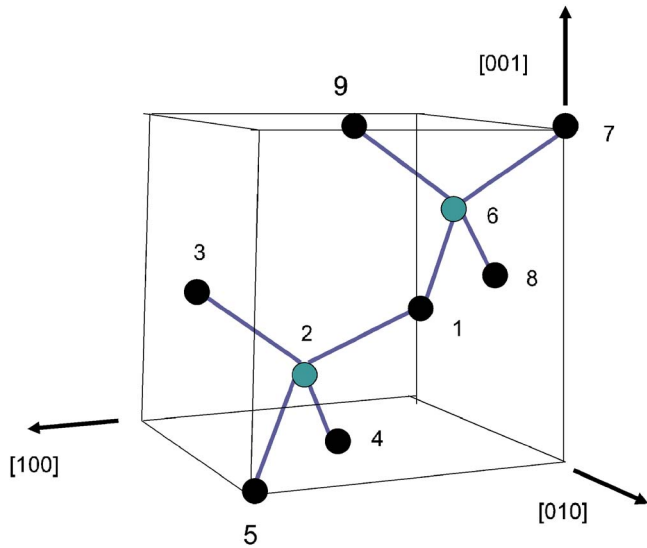


FIG. 2. (Color online) Illustration of the nine atom surface unit cell for the surface with a [010] normal of a diamond cubic crystal. Black atoms represent fcc lattice A, while green atoms represent the interpenetrating fcc lattice B. The drawn bonds connect atoms in fcc lattice B to atoms in fcc lattice A.

$$\gamma = \frac{1}{\Gamma_0} \left[\sum_{j=2,6} V_{1j}(r_{1j}) + \sum_{k=1,7,8,9} V_{6k}(r_{6k}) + \sum_{m=1,3,4,5} V_{2m}(r_{2m}) \right], \quad (17)$$

where Γ_0 is the area per atom on the surface. Following Eq. (9), we express the bond lengths for the surface unit cell as

$$\begin{aligned} r_{1j} &= |\mathbf{r}_{1j}| = |\mathbf{F}(\mathbf{R}_{1j} + \mathbf{\Xi}^s)|, \quad j = 2, 6, \\ r_{6k} &= |\mathbf{r}_{6k}| = |\mathbf{F}(\mathbf{R}_{6k} + \mathbf{\Xi}^s)|, \quad k = 1, 7, 8, 9, \\ r_{2m} &= |\mathbf{r}_{2m}| = |\mathbf{F}(\mathbf{R}_{2m} + \mathbf{\Xi}^s)|, \quad m = 1, 3, 4, 5. \end{aligned} \quad (18)$$

Incorporating the bond lengths that have been modified by the deformation gradient \mathbf{F} and the internal degrees of freedom $\mathbf{\Xi}^s$ in Eq. (18) creates a modified surface energy density $\tilde{\gamma}(\mathbf{C})$ from Eq. (17), where the surface energy density can be modified analogously to the procedure outlined previously for the bulk energy density in Eqs. (11) and (12) to enforce the energy minimizing condition

$$\frac{\partial \tilde{\gamma}}{\partial \mathbf{\Xi}^s} = 0, \quad (19)$$

where $\mathbf{\Xi}^s$, similar to the meaning in the bulk case in Eq. (12), represents the deformation of the surface internal degrees of freedom necessary to minimize the surface energy. Using the modified surface energy density $\tilde{\gamma}(\mathbf{C})$, we arrive at the expression for the surface PK2 stress $\mathbf{S}^s(\mathbf{C})$, where the superscript s here and later indicates surface values

$$\mathbf{S}^s(\mathbf{C}) = 2 \frac{\partial \tilde{\gamma}(\mathbf{C})}{\partial \mathbf{C}}. \quad (20)$$

Similarly, the surface tangent modulus can be written as

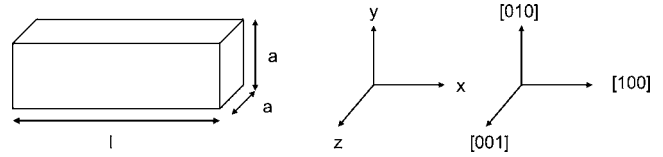


FIG. 3. Nanowire geometry considered for numerical examples.

$$\mathbf{C}_{IJKL}^s = M_{IJKL}^s - A_{IJP}^s A_{KLQ}^s (\mathbf{D}^{-1})_{PQ}^s, \quad (21)$$

where

$$M_{IJKL}^s = 4 \frac{\partial^2 \tilde{\gamma}}{\partial \mathbf{C}_{IJ}^s \partial \mathbf{C}_{KL}^s},$$

$$D_{pq}^s = \frac{\partial^2 \tilde{\gamma}}{\partial \mathbf{\Xi}_p^s \partial \mathbf{\Xi}_q^s},$$

$$A_{IJP}^s = 2 \frac{\partial^2 \tilde{\gamma}}{\partial \mathbf{C}_{IJ}^s \partial \mathbf{\Xi}_P^s}. \quad (22)$$

C. Finite element eigenvalue problem for nanowire resonant frequencies

The equation describing the eigenvalue problem for continuum elastodynamics is written as

$$(\mathbf{K} - \omega^2 \mathbf{M})\mathbf{u} = 0, \quad (23)$$

where \mathbf{M} is the mass matrix and \mathbf{K} is the stiffness matrix of the discretized FE equations; the solution of the eigenvalue problem described in Eq. (23) gives the resonant frequencies f , where $f = \omega/2\pi$ and the corresponding mode shapes \mathbf{u} . We note that the stiffness matrix \mathbf{K} contains the effects of both material and geometric nonlinearities through a consistent linearization about the finitely deformed configuration.

We emphasize that the addition of the surface energy terms in Eq. (16) leads naturally to the incorporation of the surface stresses in the FE stiffness matrix \mathbf{K} , which then leads to the dependence of the resonant frequencies f on the surface stresses. The eigenvalue problem was solved using the Sandia-developed package TRILINOS,³² which was incorporated into the simulation code TAHOE.³³

III. NUMERICAL EXAMPLES

All numerical examples were performed on three-dimensional, single crystal silicon nanowires of length l that have a square cross section of width a as illustrated in Fig. 3. Three different parametric studies are conducted in this work, which consider nanowires with constant cross-sectional area (CSA), constant length, and constant SAV (SAV); the geometries are summarized in Table I.

All wires had a $\langle 100 \rangle$ longitudinal orientation with unreconstructed $\{100\}$ transverse surfaces and had either fixed/free (cantilevered) boundary conditions, where the left ($-x$) surface of the wire was fixed while the right ($+x$) surface of the wire was free, or fixed/fixed boundary conditions, where both the left ($-x$) and right ($+x$) surfaces of the wire were fixed. All FE simulations were performed using the stated

TABLE I. Summary of geometries considered: constant SAV ratio, constant length, and constant CSA. All dimensions are in nanometers (nm).

Constant SAV	Constant length	Constant CSA
$64 \times 16 \times 16$	$240 \times 8 \times 8$	$64 \times 16 \times 16$
$110 \times 15.2 \times 15.2$	$240 \times 12 \times 12$	$128 \times 16 \times 16$
$170 \times 14.9 \times 14.9$	$240 \times 18 \times 18$	$256 \times 16 \times 16$
$230 \times 14.7 \times 14.7$	$240 \times 24 \times 24$	$384 \times 16 \times 16$
$290 \times 14.5 \times 14.5$	$240 \times 30 \times 30$	$512 \times 16 \times 16$

boundary conditions without external loading and utilized regular meshes of eight-node hexahedral elements. The bulk and surface energy densities in Eqs. (8) and (17) were calculated using Tersoff T3 parameters,²⁸ while the bulk and surface FE stresses were found using Eqs. (13) and (20).

Regardless of boundary condition, the nanowires are initially out of equilibrium due to the presence of the surface stresses. For fixed/free nanowires, the free end expands in tension to find an energy minimizing configuration under the influence of surface stresses. To illustrate this, we compare the energy minimized positions of the $128 \times 16 \times 16$ nm fixed/free nanowire using the SCB model to a benchmark molecular statics (MS) calculation performed using the Tersoff T3 potential with LAMMPS (Ref. 34) MS code. As seen in Fig. 4, the SCB model, which required only 16 393 FE nodes, gives a very accurate description of the minimum energy configuration due to surface stresses as compared to the MS calculation, which required more than 1.7×10^6 atoms. We note that the tensile strain induced in the nanowires due to the surface stresses is about 0.1%.

As noted previously, no external forces were applied to obtain the results seen in Fig. 4; all deformation is solely due

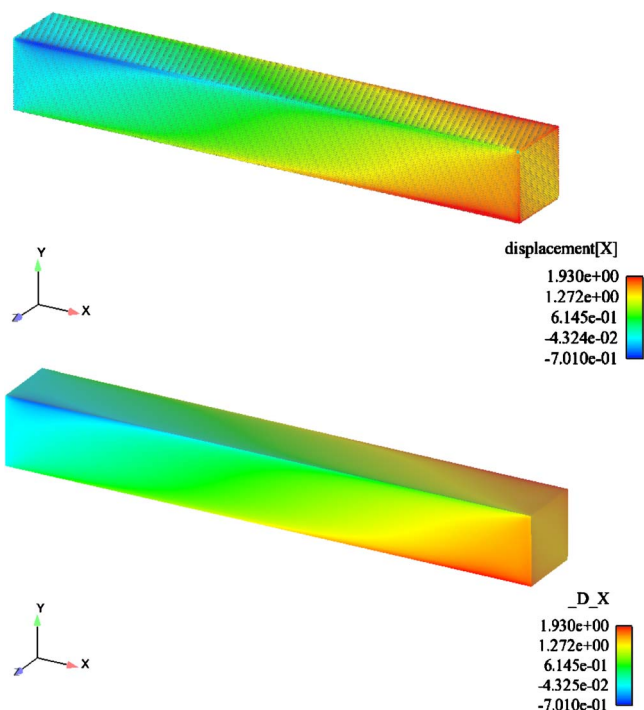


FIG. 4. (Color online) Minimum energy configuration of a fixed/free $128 \times 16 \times 16$ nm silicon nanowire due to surface stresses as predicted by (top) MS calculation, (bottom) SCB calculation.

TABLE II. Summary of constant CSA nanowire fundamental resonant frequencies for fixed/free boundary conditions as computed from: (1) The analytic solution given by Eq. (24), (2) BCB, and (3) SCB calculations. All frequencies are in megahertz (MHz), the nanowire dimensions are in nm.

Geometry	Eq. (24)	BCB	SCB
$64 \times 16 \times 16$	3933	3912	4008
$128 \times 16 \times 16$	983	990	1013
$256 \times 16 \times 16$	246	248	253
$384 \times 16 \times 16$	109	110	112
$512 \times 16 \times 16$	62	62	63

to surface stresses. In analyzing the results in Fig. 4, we emphasize that the SCB model accurately predicts the tensile expansion of the free end due to surface stresses, in addition to capturing the inhomogeneous nature of the tensile expansion, which occurs due to the noncentrosymmetric nature of the DC silicon lattice. The results are in agreement with first principles calculations,^{11,21} which also indicate that $\langle 100 \rangle$ silicon nanowires with $\{100\}$ surfaces have compressive surface stresses that cause the nanowires to expand.

Fixed/fixed nanowires, on the other hand, are constrained such that the nanowire is unable to expand due to the boundary conditions. The boundary condition constraint therefore causes the minimum energy configuration of fixed/ fixed nanowires to be a state of compression, which we will demonstrate is critical to understanding how surface stresses and boundary conditions couple to alter the resonant properties of fixed/ fixed nanowires as compared to continuum beam theory predictions.

Once the minimum energy configuration for either boundary condition is known, the eigenvalue problem described in Eq. (23) is solved using the FE stiffness matrix from the equilibrated (deformed) nanowire configuration to find the resonant frequencies. Resonant frequencies were also found using the standard BCB model (without surface stresses) on the same geometries for comparison to quantify how surface stresses change the resonant frequencies as compared to the bulk material for a given geometry and boundary condition. For all resonant frequencies reported in this work, the fundamental or lowest mode frequencies corresponded to a standard bending mode of deformation.

A. Constant cross-sectional area

To validate the accuracy of the calculations for the BCB material, we compare in Tables II and III the BCB and SCB

TABLE III. Summary of constant CSA nanowire fundamental resonant frequencies for fixed/ fixed boundary conditions as computed from: (1) The analytic solution given by Eq. (25), (2) BCB, and (3) SCB calculations. All frequencies are in MHz, the nanowire geometry is in nm.

Geometry	Eq. (25)	BCB	SCB
$64 \times 16 \times 16$	24 842	21 618	22 165
$128 \times 16 \times 16$	6211	6074	6166
$256 \times 16 \times 16$	1553	1565	1528
$384 \times 16 \times 16$	690	698	635
$512 \times 16 \times 16$	388	393	317

resonant frequencies to those obtained using the well-known analytic solutions for the fundamental resonant frequency for both fixed/free (cantilevered) and fixed/fixed beams.³⁵ For the fixed/free beam

$$f_0 = \frac{B_0^2}{2\pi l^2} \sqrt{\frac{EI}{\rho A}}, \quad (24)$$

where $B_0 = 1.875$ for the fundamental resonant mode, E is the modulus for silicon in the $\langle 100 \rangle$ direction, which can be found to be 90 GPa,²⁸ I is the moment of inertia, l is the nanowire length, A is the cross-sectional area, and ρ is the density of silicon. The FE calculations used to calculate the BCB and SCB resonant frequencies involved regular meshes of eight-node hexahedral elements; the mesh sizes ranged from about 8000 to 65 000 nodes for the constant CSA nanowires considered.

The BCB resonant frequencies compare quite well to those predicted by the analytic formula, with increasing accuracy for increasing aspect ratio l/a , as would be expected from beam theory. We note that the SCB resonant frequencies are consistently larger than the BCB resonant frequencies and thus the analytic solution; reasons for this trend will be discussed later.

For the fixed/fixed beam, the analytic solution is given as³⁵

$$f_0 = \frac{i^2 \pi}{2l^2} \sqrt{\frac{EI}{\rho A}}, \quad (25)$$

where $i \approx 1.5$ is a mode shape factor for fixed/fixed beams. Table III shows that the BCB and analytic solutions again agree nicely. However, in contrast to the fixed/free case, the SCB resonant frequencies are found to decrease with increasing aspect ratio relative to the bulk material; again, reasons for this will be discussed later. A key point to emphasize here is that due to the accuracy of the BCB results for both boundary conditions as compared to the analytic solutions, normalizing the SCB resonant frequencies by the BCB resonant frequencies can be considered to be equivalent to normalizing by the solution expected from continuum beam theory.

Figure 5(a) shows the normalized resonant frequencies f_{scb}/f_{bulk} plotted against both the nanowire aspect ratio l/a and the SAV ratio, for both fixed/fixed and fixed/free boundary conditions. As can be observed, the surface stress effects on the resonant frequencies depend strongly upon the corresponding boundary conditions. For the fixed/free nanowires, the resonant frequencies predicted using the SCB model are about 2% higher than those of the BCB model for all aspect ratios. In contrast, the fixed/fixed nanowires show completely different behavior. In that case, the resonant frequencies predicted by the SCB model dramatically decrease with increasing aspect ratio l/a , with the resonant frequencies due to surface stress decreasing to nearly 20% lower than the corresponding bulk material when the aspect ratio $l/a > 30$.

The resonant frequency calculations are also plotted with respect to the SAV ratio in Fig. 5(b). As can be seen, the

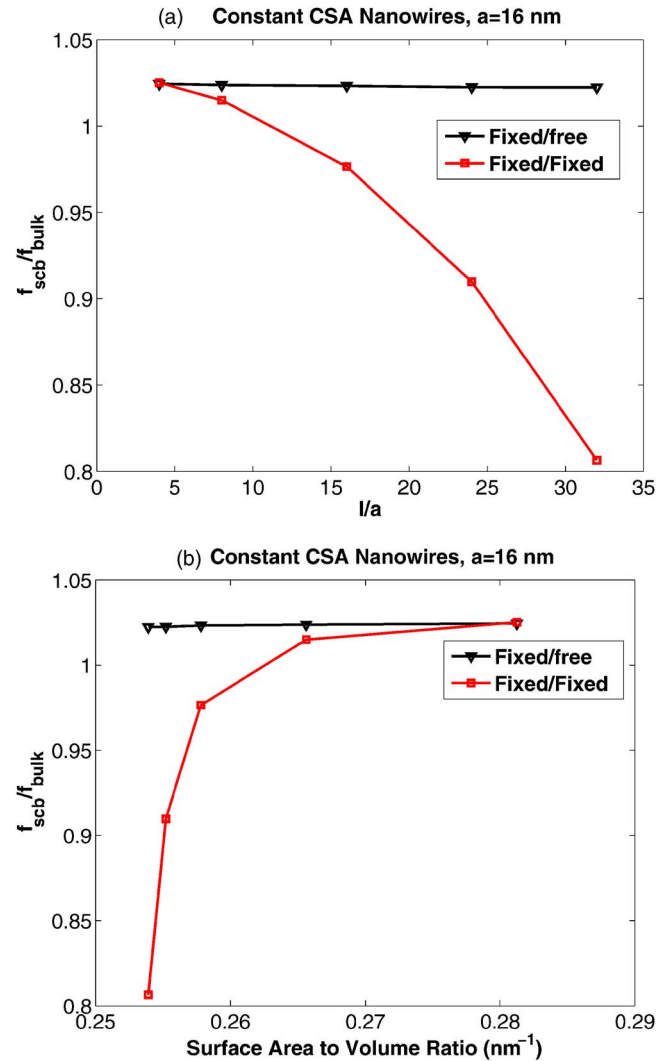


FIG. 5. (Color online) Normalized resonant frequencies for constant CSA silicon nanowires.

fixed/free nanowires show little variation with the SAV ratio, while the fixed/fixed nanowires show a decrease in resonant frequency with decreasing SAV ratio.

B. Constant length

We next investigate the resonant frequencies of nanowires in which the length of the nanowire was fixed at 240 nm, while the square cross section was varied in size. The FE calculations to determine the resonant frequencies required mesh sizes ranging from about 13 000 nodes for the smallest (8 nm) cross section to about 71 000 nodes for the largest (30 nm) cross section considered.

As with the constant CSA nanowires, we plot the f_{scb}/f_{bc} ratio against both the aspect ratio l/a and the SAV ratio in Fig. 6(a). When plotted against the aspect ratio l/a , the trends for the constant length nanowires are similar to those of the constant CSA nanowires, particularly for the fixed/fixed boundary conditions, for which surface stresses cause the resonant frequencies to decrease rapidly with increasing l/a . In fact, for $l/a=30$ for the 8 nm cross-section nanowire, surface stresses cause the resonant frequency to be less than 65% of the bulk value. The surface stresses cause a

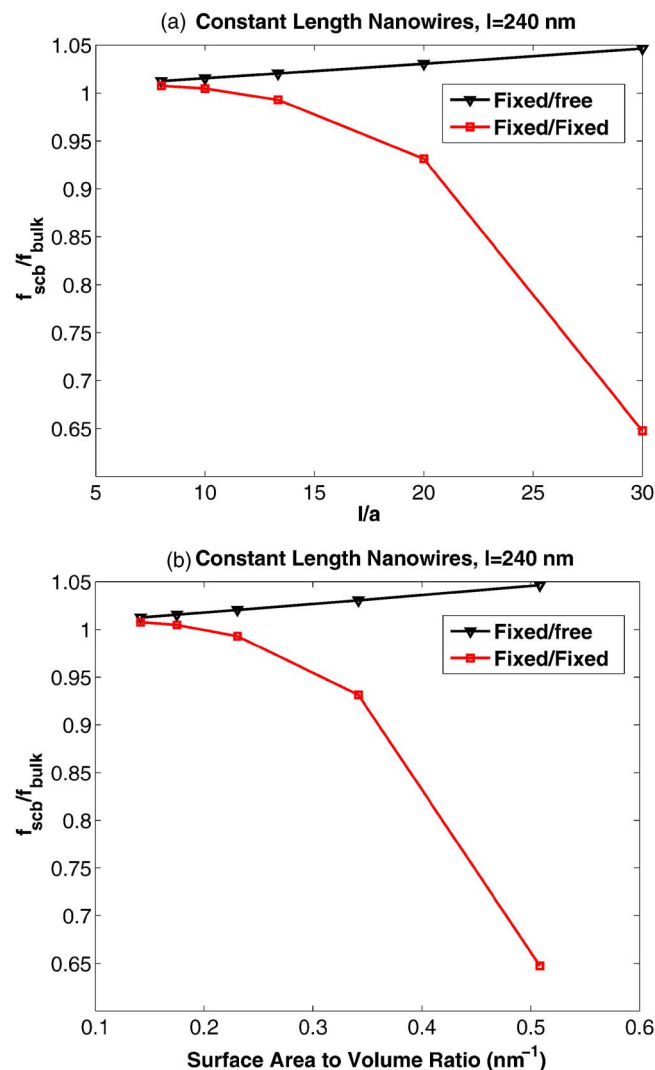


FIG. 6. (Color online) Normalized resonant frequencies for constant length silicon nanowires.

slightly different trend for the fixed/free case. There, the resonant frequencies are observed to increase slightly with respect to the bulk value with increasing l/a , while the trend was a very minute decrease in the constant CSA case.

However, when plotted against the SAV ratio, as in Fig. 6(b), the results for constant length nanowires differ strongly from the constant CSA nanowires. In particular, the result is most noticeable for the fixed/fixed nanowires; in the constant CSA case, surface stresses caused an increase in resonant frequency with increasing SAV ratio. However, for the constant length nanowires, the opposite trend is observed; the surface stresses cause the resonant frequencies to decrease with increasing SAV ratio. The trends are also reversed, though not as dramatically, for the fixed/free boundary conditions.

C. Constant surface area to volume ratio

Due to the variation in surface stress and boundary condition effects on the nanowire resonant frequencies, we consider those coupled effects for nanowires that have the same SAV ratio, 0.28 nm^{-1} . The FE mesh sizes ranged in this case

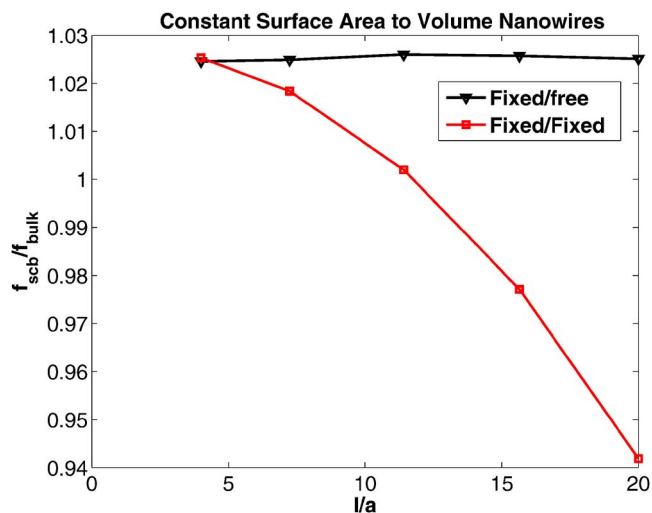


FIG. 7. (Color online) Normalized resonant frequencies for constant SAV silicon nanowires.

from about 15 000 nodes (for the 15.2 nm cross-section nanowire) to about 41 000 nodes (for the 14.5 nm cross-section nanowire).

Because the SAV ratio is kept constant, we plot the resonant frequencies for both boundary conditions only against the nanowire aspect ratio l/a in Fig. 7. Figure 7 thus shows one of the fundamental findings of this work, in that the resonant frequencies of fixed/fixed silicon nanowires do not, due to surface stresses, depend on the SAV ratio. The results for the fixed/free nanowires are more ambiguous judging solely from Fig. 7. However, Figs. 5(a) and 6(a) indicate that the resonant frequencies of fixed/free silicon nanowires, similar to fixed/fixed silicon nanowires, do not scale according to SAV ratio.

In particular, in all cases, it appears that the nanowire aspect ratio l/a is a much stronger predictor of how the boundary conditions and surface stresses couple to vary the resonant frequencies as compared to the corresponding bulk material than the SAV ratio. This finding corresponds to results recently published by Verbridge *et al.*³⁶ and Petrova *et al.*³⁷ The Verbridge work analyzed the resonant properties of SiN nanostrings, with cross-sectional dimensions around 100 nm. While the surface stress effects observed in the present work are unlikely to have a significant impact on 100 nm cross-section nanowires, it is interesting that even when surface effects become significant, as they do for the nanowires considered in the present work, that the resonant frequencies, and thus the elastic properties, are largely independent of SAV ratio. The Petrova work offers a comparison at a different length scale (cross sections on the order of 10–20 nm) and for a different material, gold. However, that work also found weak dependence of the resonant frequencies and thus elastic properties on the SAV ratio; these results, on different materials at different sizes, lend credibility to the results obtained in the present work.

IV. DISCUSSION AND ANALYSIS

We now present an analysis of the boundary condition and surface stress effects on the nanowire elastic properties,

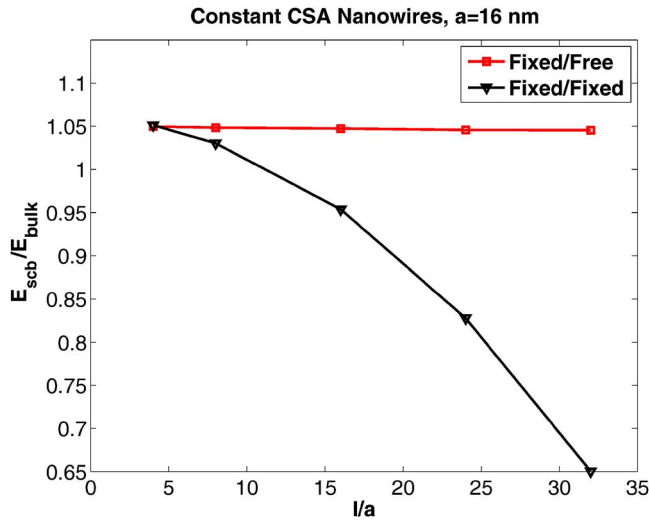


FIG. 8. (Color online) Normalized Young's modulus for both fixed/fixed and fixed/free boundary conditions for constant CSA nanowires.

and in particular the Young's modulus. To calculate the Young's modulus, we utilize the beam theory expressions that relate the resonant frequencies to the modulus in Eqs. (24) and (25). The beam theory expressions for the modulus are utilized as they are also ubiquitous in the experimental literature to calculate the Young's modulus for nanostructures.^{3,7,16,36–38}

Figure 8 depicts the variation in the Young's modulus, as normalized by the bulk value, for both the fixed/fixed and fixed/free constant CSA nanowires. As can be observed, the Young's modulus for the fixed/free case shows about a 5% variation from the bulk value, which can be expected from the fact that the fixed/free resonant frequencies, when bulk normalized, also showed a small increase with respect to the bulk resonant frequencies.

However, there is a dramatic variation in the fixed/fixed Young's modulus with increasing aspect ratio l/a , as shown in Fig. 8. In particular, due to the nature of the resonance formula in Eq. (25), the modulus that is calculated is actually significantly reduced as compared to the bulk Young's modulus than the bulk-normalized resonant frequencies. For example, $f_{scb}/f_{bulk}=0.81$ for $l/a=30$, as seen in Fig. 5(a). However, when surface stresses are accounted for, the Young's modulus drops to only 65% of the bulk modulus when $l/a=32$.

Furthermore, this observed reduction of the Young's modulus has been observed in other theoretical studies for fixed/fixed silicon nanowires. In particular, we note the recent density functional theory studies by Lee and Rudd for ultrasmall (<4 nm) fixed/fixed silicon nanowires,¹¹ which also predicted a decrease in Young's modulus due to the fact that the surface stresses in conjunction with the fixed/fixed boundary conditions cause the nanowire to exist in a state of compression; we note that the variation of the Young's modulus accounting for length was not performed in that work. Molecular dynamics simulations of the resonant frequencies of fixed edge silicon oxide nanoplates by Broughton *et al.*³⁹ also revealed a distinct reduction in the resonant frequencies with decreasing size.

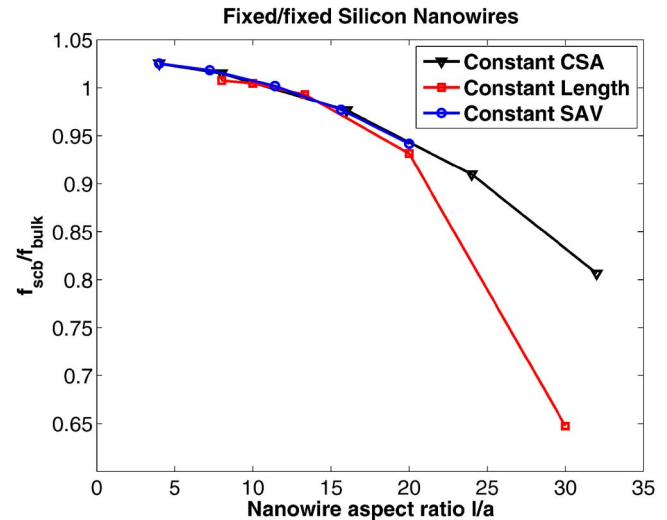


FIG. 9. (Color online) Normalized resonant frequencies for fixed/fixed constant CSA, SAV, and length nanowires plotted against the nanowire aspect ratio.

We also seek to quantify the variations due to surface stresses in the resonant frequencies for the fixed/fixed case. To do so, Fig. 9, which plots the normalized resonant frequencies f_{scb}/f_{bulk} for all fixed/fixed nanowires (constant CSA, length, SAV) against the nanowire aspect ratio l/a , demonstrates one of the major findings of this work. As can be seen, for the nanowire sizes considered in this work, the resonant frequencies for all nanowires as compared to the resonant frequencies of the bulk material overlap on a similar curve as a function of the aspect ratio, with the trend being a decreasing resonant frequency with increasing aspect ratio. The enhanced effect of surface stresses for the constant length nanowire with aspect ratio of $l/a=30$ is likely due to the fact that it was the smallest cross section considered, i.e., 8 nm, where the surface stress effects are particularly strong. Figure 9 can therefore serve as a design guide for predicting how surface stresses will change the resonant frequencies of nanowires as compared to the continuum beam theory in Eq. (25) which does not account for surface effects.

We attempted to determine similar relationships for the fixed/free nanowires in linking the observed variations of the nanowire resonant frequencies due to surface stresses to geometric parameters. Unfortunately, as illustrated in Fig. 10, such a relationship was not found in this work. We also studied the variation in resonant frequencies due to surface stresses as compared to the tensile strain in the nanowires, but a similarly inconclusive result was obtained. However, Fig. 10 does indicate that surface stresses are likely not to strongly impact (more than 2%) the resonant frequencies of fixed/free nanowires unless very small cross sectional areas (<10 nm) and large aspect ratios are utilized.

A. Comparison to experiment

An extensive literature search has revealed that most studies utilizing resonating silicon nanowires involve nanowires with cross-sectional sizes generally exceeding 50 nm.^{3,7,38} At those sizes, both the experimental results and extrapolation of the current SCB results indicate that surface

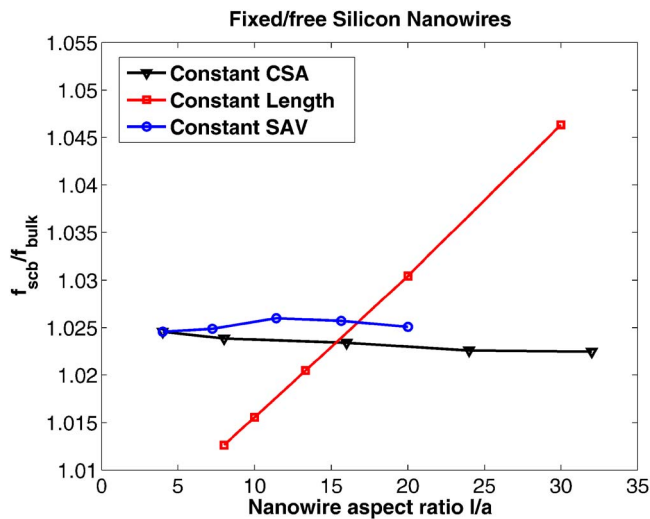


FIG. 10. (Color online) Normalized resonant frequencies for fixed/free constant CSA, SAV, and length nanowires plotted against the nanowire aspect ratio.

effects will not have a dominant role on the resonant frequencies, and that continuum beam theory should be valid for interpreting the resonant properties.

We did find one study involving the resonant properties of sub-30 nm cross-section silicon nanowires, that of Li *et al.*¹⁶ The silicon nanowires in that work were of the $\langle 110 \rangle$ orientation and were fabricated in the fixed/fixed configuration. The nanowires were found to have a sharp decrease in Young's modulus, with a 53 GPa Young's modulus reported for 12 nm diameter nanowires. In comparison, using the results in Fig. 8, we find that the SCB model predicts a 58.5 GPa Young's modulus for a 16 nm cross-section $\langle 100 \rangle$ nanowire. We note that a direct comparison cannot be made due to the fact that the nanowires in the present work were axially aligned in the $\langle 100 \rangle$ direction.

Two other studies involving the mechanical properties of sub-30 nm cross-section silicon nanowires were found, with both involving tensile deformation. Kizuka *et al.*¹⁷ used an AFM to perform tensile elongation of single crystal $\langle 100 \rangle$ silicon nanowires with cross sections less than 10 nm; the measured Young's modulus was on the order of 18 GPa, which is considerably smaller than the 90 GPa Young's modulus for bulk $\langle 100 \rangle$ silicon.

More recently, Han *et al.*¹⁸ also performed *in situ* transmission electron microscopy observation of the tensile failure of $\langle 110 \rangle$ silicon nanowires. Nanowire sizes down to 15 nm cross sections were considered; using the activation energy for dislocation nucleation, they also obtained a strong size dependence in the Young's modulus, with a modulus value of 55 GPa reported for 15 nm cross-section nanowires. Again, the 58.5 GPa modulus obtained using the SCB model for 16 nm cross-section $\langle 100 \rangle$ nanowires agrees well, though as before, a direct comparison cannot be made due to the different crystallographic orientations.

Despite the small amount of experimental data to which to compare the present results, the present results are qualitatively consistent with available experimental data^{16–18} and

theoretical results^{11,39} in predicting a relative decrease in resonant frequencies, and thus Young's modulus, for fixed/fixed nanowires.

V. CONCLUSIONS

In conclusion, we have utilized the recently developed surface Cauchy–Born model to quantify how boundary conditions and surface stresses couple to cause variations in the resonant properties of silicon nanowires as compared to those expected from continuum beam theory. The resonant properties were found through solution of a standard finite element eigenvalue problem, where the effects of surface stresses are naturally captured within the finite element stiffness matrix. The usage of a three-dimensional nonlinear finite element formulation thus efficiently enabled the analysis of a variety of nanowire geometries to quantify surface stress effects on nanowire resonant properties.

With regards to the effects of surface stresses on the silicon nanowire resonant frequencies, we have found that: (1) Surface stresses cause significant deviations in the resonant frequencies of nanowires as compared to those that are found using standard continuum beam theory with bulk material properties, with the deviation having a different trend depending on whether fixed/fixed or fixed/free boundary conditions are used. We find that the resonant frequencies of nanowires with cross-sectional lengths greater than about 30 nm show little deviation from those predicted from continuum beam theory. We also find that surface stresses most strongly impact the resonant properties of fixed/fixed silicon nanowires, which are found to decrease substantially as compared to predictions from continuum beam theory. In contrast, surface stresses do not cause substantial deviations from beam theory for fixed/free silicon nanowires unless nanowires with very small cross-sectional lengths (<10 nm) and large aspect ratios are considered. (2) For fixed/fixed silicon nanowires, accounting for the compressive state of stress resulting from the coupled effects of surface stresses and boundary conditions is critical to capturing the observed reductions in the resonant frequencies as compared to continuum beam theory. (3) The deviation that surface stresses cause in the resonant properties of fixed/fixed nanowires as compared to beam theory scales proportional to the nanowire aspect ratio l/a . (4) No such scaling relationship was found for surface stress effects on the resonant properties of fixed/free nanowires. (5) The present finding that the resonant properties of fixed/fixed silicon nanowires, and therefore the elastic properties such as the Young's modulus decrease with respect to the bulk value qualitatively agrees with recent experimental^{16–18} and theoretical^{11,39} results.

ACKNOWLEDGMENTS

H.S.P. gratefully acknowledges support of the NSF through Grant No. CMMI-0750395.

¹Y. Xia, P. Yang, Y. Sun, Y. Wu, B. Mayers, B. Gates, Y. Yin, F. Kim, and H. Yan, *Adv. Mater.* **15**, 353 (2003).

²H. G. Craighead, *Science* **290**, 1532 (2000).

³A. N. Cleland and M. L. Roukes, *Appl. Phys. Lett.* **69**, 2653 (1996).

⁴L. T. Canham, *Appl. Phys. Lett.* **57**, 1046 (1990).

- ⁵T. D. Stowe, K. Yasumura, T. W. Kenny, D. Botkin, K. Wago, and D. Rugar, *Appl. Phys. Lett.* **71**, 288 (1997).
- ⁶A. N. Cleland and M. L. Roukes, *Nature (London)* **392**, 160 (1998).
- ⁷X. L. Feng, R. He, P. Yang, and M. L. Roukes, *Nano Lett.* **7**, 1953 (2007).
- ⁸R. C. Cammarata, *Prog. Surf. Sci.* **46**, 1 (1994).
- ⁹J. Diao, K. Gall, and M. L. Dunn, *Nat. Mater.* **2**, 656 (2003).
- ¹⁰H. S. Park, K. Gall, and J. A. Zimmerman, *Phys. Rev. Lett.* **95**, 255504 (2005).
- ¹¹B. Lee and R. E. Rudd, *Phys. Rev. B* **75**, 195328 (2007).
- ¹²H. W. Shim, L. G. Zhou, H. Huang, and T. S. Cale, *Appl. Phys. Lett.* **86**, 151912 (2005).
- ¹³B. Ilic, Y. Yang, K. Aubin, R. Reichenbach, S. Krylov, and H. G. Craighead, *Nano Lett.* **5**, 925 (2005).
- ¹⁴A. San Paulo, J. Bokor, R. T. Howe, R. He, P. Yang, D. Gao, C. Carraro, and R. Maboudian, *Appl. Phys. Lett.* **87**, 053111 (2005).
- ¹⁵M. Tabib-Azar, M. Nassirou, R. Wang, S. Sharma, T. I. Kamins, M. S. Islam, and R. S. Williams, *Appl. Phys. Lett.* **87**, 113102 (2005).
- ¹⁶X. Li, T. Ono, Y. Wang, and M. Esashi, *Appl. Phys. Lett.* **83**, 3081 (2003).
- ¹⁷T. Kizuka, Y. Takatani, K. Asaka, and R. Yoshizaki, *Phys. Rev. B* **72**, 035333 (2005).
- ¹⁸X. Han, K. Zheng, Y. F. Zhang, X. Zhang, Z. Zhang, and Z. L. Wang, *Adv. Mater.* **19**, 2112 (2007).
- ¹⁹S. Cuenot, C. Frétygny, S. Demoustier-Champagne, and B. Nysten, *Phys. Rev. B* **69**, 165410 (2004).
- ²⁰G. Y. Jing, H. L. Duan, X. M. Sun, Z. S. Zhang, J. Xu, Y. D. Li, J. X. Wang, and D. P. Yu, *Phys. Rev. B* **73**, 235409 (2006).
- ²¹H. Balamane, T. Halicioglu, and W. A. Tiller, *Phys. Rev. B* **46**, 2250 (1992).
- ²²H. S. Park, P. A. Klein, and G. J. Wagner, *Int. J. Numer. Methods Eng.* **68**, 1072 (2006).
- ²³H. S. Park and P. A. Klein, *Phys. Rev. B* **75**, 085408 (2007).
- ²⁴P. Lu, H. P. Lee, C. Lu, and S. J. O'Shea, *Phys. Rev. B* **72**, 085405 (2005).
- ²⁵R. Dingreville, J. Qu, and M. Cherkaoui, *J. Mech. Phys. Solids* **53**, 1827 (2005).
- ²⁶A. W. McFarland, M. A. Poggi, M. J. Doyle, L. A. Bottomley, and J. S. Colton, *Appl. Phys. Lett.* **87**, 053505 (2005).
- ²⁷J. E. Sader, *J. Appl. Phys.* **89**, 2911 (2001).
- ²⁸J. Tersoff, *Phys. Rev. B* **39**, 5566 (1989).
- ²⁹E. Tadmor, M. Ortiz, and R. Phillips, *Philos. Mag. A* **73**, 1529 (1996).
- ³⁰Z. Tang, H. Zhao, G. Li, and N. R. Aluru, *Phys. Rev. B* **74**, 064110 (2006).
- ³¹H. S. Park and P. A. Klein, *Comput. Methods Appl. Mech. Eng.* (accepted).
- ³²TRILINOS, <http://software.sandia.gov/trilinos/index.html>, 2007.
- ³³TAHOE, <http://tahoe.ca.sandia.gov>, 2007.
- ³⁴WARP, <http://www.cs.sandia.gov/~sjplimp/lammps.html>, 2006.
- ³⁵W. Weaver, S. P. Timoshenko, and D. H. Young, *Vibration Problems in Engineering* (Wiley, New York, 1990).
- ³⁶S. S. Verbridge, J. M. Parpia, R. B. Reichenbach, L. M. Bellan, and H. G. Craighead, *J. Appl. Phys.* **99**, 124304 (2006).
- ³⁷H. Petrova, J. Perez-Juste, Z. Y. Zhang, J. Zhang, T. Kosel, and G. V. Hartland, *J. Mater. Chem.* **16**, 3957 (2006).
- ³⁸D. W. Carr, S. Evoy, L. Sekaric, H. G. Craighead, and J. M. Parpia, *Appl. Phys. Lett.* **75**, 920 (1999).
- ³⁹J. Q. Broughton, C. A. Meli, P. Vashishta, and R. K. Kalia, *Phys. Rev. B* **56**, 611 (1997).